SUPPLEMENTARY INFORMATION
DOI: 10.1038/NNANO.2016.96

Three-dimensional mapping and regulation of action potential propagation in nanoelectronics-innervated tissues

Xiaochuan Dai, Wei Zhou, Teng Gao, Jia Liu & Charles M. Lieber

This file includes:

DOI: 10.1038/NNANO.2016.96

Supplementary Methods

1. Free-standing nanoelectronic scaffold fabrication

1.1 Silicon nanowire synthesis

Silicon nanowires were synthesized by a gold nanocluster-catalyzed vapor-liquid-solid growth method reported previously[1]. Briefly, the growth substrate (p-type Si, 0.005 Ω cm, 600 nm oxide, Nova Electronic Materials, LLC., Flower Mound, TX) was cleaned and made hydrophilic by oxygen plasma (100 W, 3 min), treated with poly-L-lysine solution (0.1%, Ted Pella, Inc., Redding, CA) for 5 min, and then rinsed thoroughly with deionized (DI) water. 30 nm gold nanoparticles (Ted Pella, Inc., Redding, CA) were dispersed on growth substrates for 2 min and then then rinsed thoroughly with DI water. Nanowire growth was carried out at 450 °C under a constant pressure of 30 Torr with SiH_4 (2 standard cubic centimeters per minute (SCCM), 99.9+%, Voltaix, Branchburg, NJ), diluted B_2H_6 (2.5 SCCM, 97 ppm in hydrogen, Voltaix, Branchburg, NJ), and Argon (10 SCCM, 99%, Matheson Tri-Gas, Manchester, NH) as silicon-reactant, dopant (4000:1 silicon:boron feed-in ratio), and carrier gases, respectively. The 30 min growth time was chosen to yield an average nanowire length of 30 μm, suitable for contact-printing with plasma-based surface treatment critical to our approach (see Supplementary Methods, 1.2).

1.2 Nanowire contact-printing

Fabrication of the free-stranding nanoelectronics requires assembly of silicon nanowires onto a polymer surface. Specific challenges of assembly include (1) modification of the polymer surface to enhance its affinity to the distinct surface properties of the silicon nanowires; (2) high density assembly to enable high-yield device fabrication while miniaturizing the device dimensions; and (3) photolithography defined deterministic assembly to enable compatibility

with overall mesh fabrication processes. Our previous nanowire drop-casting method[2] yields a low nanowire density or 0.01–0.1 μm^{-1}, which precluded reducing the size of nanodevices below 100 μm without sacrificing fabrication yield. Contact-printing technique has demonstrated high-density assembly of nanowires (>10 μm^{-1}), however scratching damage to the polymer mesh structure as a result of the physical contact undermines device fabrication yields and passivation quality. To overcome these critical issues we introduced a plasma-based surface treatment as follows (Supplementary Fig. 1):

(1) A 350 nm thick layer of SU-8 photoresist (2000.5, MicroChem Corporation, Newton, MA) was spin coated over the entire substrate at 4000 rpm for 2 min, followed by prebaking at 65 and 95 °C for 1 and 3 min, respectively (Supplementary Fig. 1a). Photolithography (PL) was used to define an array of rectangular pads (Supplementary Fig. 1b), which corresponding to one device site.

(2) Oxygen plasma treatment (30 W, 20 s) was used to treat the SU-8 surface, thereby making it hydrophilic (Supplementary Fig. 1c), which is important for achieving high density nanowire assembly.

(3) The substrate was immediately mounted onto a micromanipulator controlled stage, coated with ca. 40 μL oil (heavy mineral oil, 330760, Sigma-Aldrich Corporation, Atlanta, GA). A silicon nanowire growth substrate (1.2 cm × 1.2 cm) (see Supplementary Methods, 1.1), which was also treated with oxygen plasma (100 W, 1 min), was brought into contact with the receiver substrate (under pressure, 4.8 N cm^{-2}). The receiver substrate was then translated at 5 mm min^{-1} with respect to the fixed growth substrate to transfer aligned nanowires on the receiver substrate due to interactions between surfaces of plasma-treated nanowires and SU-8 (Supplementary Fig. 1d). The target substrate was gently rinsed with hexane to remove oil.

DOI: 10.1038/NNANO.2016.96

Without oxygen plasma treatment of the SU-8, the density of transferred nanowires, <0.2 μm^{-1}, is similar to previous drop-cast method[2] and did not meet the goals of the work. With oxygen plasma treatment the density of transferred nanowire was 1–5 μm^{-1}.

(4) The receiver substrate was then post-baked at 65 and 95 °C for 1 and 3 min, respectively (Supplementary Fig. 1e). SU-8 cross-linking occurs in UV and plasma patterned regions (rectangular pads and intermediate surface).

(5) The substrate was placed upside-down in SU-8 developer (MicroChem Corporation, Newton, MA) for 1 min to remove the non-cross-linking regions (Supplementary Fig. 1f), and then put into a sonicator (500D, Crest Ultrasonics Corp., Trenton, NJ) for 10 s sonication at 24 W. The sonication removes all silicon nanowires except those transferred to the array of PL defined rectangular SU-8 pads (Supplementary Fig. 1g).

(6) The target substrate was rinsed with isopropanol and then hard baked at 180 °C for 20 min (Supplementary Fig. 1h).

For the above transfer methodology, the silicon nanowire density on SU-8 was 1–5 μm^{-1} and device yields of >86 and >95% for deterministic source/drain electrode widths of 1 and 2 μm, respectively, where the electrodes are patterned relative to the original design and without preexisting knowledge of specific nanowire positions.

1.3 Photolithography-based fabrication of the nanoelectronic scaffolds

The free-standing nanoelectronic mesh scaffolds were fabricated on Ni/SiO_2/Si substrates via PL and then released by Ni etching, using similar methods as described previously[2, 3]. Key steps used in the photolithography-based fabrication were as follows (Supplementary Figs. 2a–f):

(1) PL and metal deposition was used to define a nickel metal film (100 nm) on the oxide surface of a silicon substrate (p-type Si, 0,005 Ω cm, 600 nm oxide, Nova Electronic Materials, LLC.,

Flower Mound, TX). The nickel serves as the relief layer, which when removed yields the free-standing scaffolds; steps 2–6 were carried out on the surface of nickel layer (Supplementary Figs. 2a–b).

(2) Contact-printing (see Supplementary Methods, 1.2) was carried out to fabricate an array of SU-8 rectangular pads with aligned silicon nanowires deterministically transferred onto these SU-8 structures (Supplementary Fig. 2c).

(3) A 350 nm thick layer of SU-8 photoresist was spin-coated at 4000 rpm for 2 min followed by prebaking at 65 and 95 °C for 1 and 3 min, respectively. PL was used to pattern SU-8 layer into the designed mesh structure (Supplementary Fig. 2d), which connects the nanowire/SU-8 array of rectangular pads with nanowire elements, and serves as lower passivation layer for metal interconnects that address the nanowire nanoelectronic device network. The structure was post baked, developed, and hard backed by the same procedures described in Supplementary Methods 1.2.

(4) Primer MCC and LOR3A (MicroChem Corporation, Newton, MA) were sequentially spin-coated at 4000 rpm for 2 min followed by prebaking at 185 °C for 5 min. Photoresist S1805 (MicroChem Corporation, Newton, MA) was spin-coated at 4000 rpm for 2 min, prebaked at 115 °C for 2 min, and then PL and thermal evaporation were used to define and deposit the metal source/drain contacts and interconnects (Cr/Pd/Cr, 1.5/50/1.5 nm) followed by lift off in Remover PG (MicroChem Corporation, Newton, MA) at 55 °C for 30–60 min; the metal layer is shown in Supplementary Fig. 2e.

(5) Another 350 nm layer of SU-8 photoresist was spin-coated at 4000 rpm for 2 min, prebaked at 65 and 95 °C for 1 and 3 min, respectively, and then PL was used to pattern the top SU-8 mesh structure (Supplementary Fig. 2f), which overlaps with the bottom mesh layer and

DOI: 10.1038/NNANO.2016.96

passivates the metal source/drain contacts and interconnects. The structure was post baked, developed, and hard baked using the same procedures as described above.

(6) The free-standing macroporous nanoelectronic mesh scaffolds were released from the substrate by etching the nickel layer (Nickel Etchant TFB, Transene Company, Inc., Danvers) for 60–120 min at 25 °C. The input/output (I/O) end of the free-standing mesh scaffold remains attached to the substrate. Free-standing nanoelectronic mesh scaffolds were rinsed three times with DI water and stored in DI water.

The resulting nanoelectronic mesh scaffolds consisted of four 4 × 4 FET arrays, which yields 4 × 4 × 4 array of devices within the final folded 3D scaffolds (see Supplementary Methods, 2.1) for 3D mapping (Supplementary Fig. 3). The layouts of the scaffolds can be readily changed with different lithography mask designs without affecting the basic principles of our fabrication strategy, and thus allows for facile changes in the number and geometric distribution of devices for different mapping requirements.

1.4 Nanoelectronic scaffold characterization

1.4.1 Optical characterization

Optical photographs were acquired by a SLR digital camera (Canon U.S.A., Inc., Melville, NY) and bright-field/dark-field microscope images were acquired by Andor iXonEM 885 CCD camera through Olympus FSX100 microscope system and recorded using Andor SOLIS (X-4238) software to characterize the free-standing nanoelectronic mesh scaffolds.

Etching the nickel relief layer (see Supplementary Methods, 1.3) yields a free-standing highly-flexible nanoelectronic mesh scaffold structure (Supplementary Fig. 4a). The four 4 × 4 FET arrays can be readily identified from photographs (green dashed-boxes, Supplementary Fig. 4a). The center-to-center distance between these arrays is 8 mm and the device pitch within the 4

× 4 arrays is 1.6 mm, although these parameters could be easily varied through changes to the lithography mask design. The size of the nanowire FET sensors (Supplementary Fig. 4a, inset), ≤100 nm × 2 μm (1–3 nanowires for 1–2 μm channel width design times 2 μm channel length), enable local point-like detection of action potentials (APs). White dashed-box in Supplementary Fig. 4a also highlights integrated parallel I/O consisting of 68 parallel electrodes (4 common source; 64 drain) for independently multiplexed addressing capability of the 64 silicon nanowire FET sensors.

1.4.2 Electrical characterization

Electrical transport measurements were carried out using a probe station (Lake Shore Cryotronics, Inc., Westerville, OH). Each nanowire FET was characterized independently to show device fabrication yield and sensitivity. Specifically, source/drain electrodes for each FET device were contacted with probes, an electrolyte gate was formed by covering the nanowire FET with a drop of phosphate-buffered saline (PBS) (1×, Corning Inc., NY), and gate potential was varied using a Ag/AgCl electrode in this electrolyte. The conductance of silicon nanowire FETs was measured with 100 mV DC bias with gate voltage varied from -0.2 – 0.2 V. The drain current was amplified with a variable-gain amplifier (1211 current preamplifier; DL Instruments, Inc.) and the output data were band pass filtered (0–6000 Hz, CyberAmp 380, Molecular Devices, Sunnyvale, CA) and recorded at an acquisition rate of 20–100 kHz using a 16-channel A/D converter (Digidata 1440A; Molecular Devices, Sunnyvale, CA). Data analysis was carried out using Origin Pro (ver. 8.1, Origin Lab Corp.) Electrical characterization yielded >95% and >86% viable nanowire FETs for the 2 and 1 μm width, respectively, electrode designs. Statistical analyses of the device performance have shown an average sensitivity of 24 μS V^{-1} and sensitivity-to-noise ratio of 1.5 mV^{-1} (Supplementary Fig. 7a). These values are suitable for

DOI: 10.1038/NNANO.2016.96

reproducible recording of extracellular APs and can exhibit better performance during the tissue culture (see Supplementary Methods, 4.2).

1.4.3 Stiffness characterization

The bending stiffness of nanoelectronic mesh scaffolds was calculated to provide design guidelines for achieving nanoelectronic scaffolds that exhibited comparable mechanical properties and feature sizes as conventional passive tissue scaffolds. The nanoelectronic mesh scaffold consists of two types of structural elements: (1) SU-8/metal/SU-8, and (2) SU-8 without metal. The SU-8/metal/SU-8 elements make up ~26% of the total length of mesh elements in the scaffold. The bending stiffness values of two types of structural elements are as follows:

(1) The bending stiffness, K_1, of the nanoelectronic SU-8/metal/SU-8 mesh elements can be expressed as[4]

$$K_1 = E_s \frac{w_1 h_1^3}{12} + (E_m - E_s)\frac{w_m h_m^3}{12} \quad \text{(S1)}$$

Where E_s is Young's modulus of SU-8, E_m is Young's modulus of contact metal (palladium, contribution from chromium is neglected due to its negligible thickness), h_1 is the total thickness of tri-layer ribbon, h_m is the thickness of metal, w_1 is the total width of ribbon and w_m is the width of metal. When $E_s =$ 2 GPa, $E_m =$ 121 GPa, $h_1 =$ 750 nm, $h_m =$ 50 nm, $w_1 =$ 4 μm, and $w_m =$ 2 μm, we can calculate $K_1 = 2.8 \times 10^{-16}$ N m^2.

(2) The bending stiffness, K_2, of SU-8 mesh elements without metal is given by[4]

$$K_2 = E_s \frac{w_2 h_2^3}{12} \quad \text{(S2)}$$

When $h_2 =$ 350 nm, $w_2 =$ 4 μm, we can calculate $K_2 =$ 2.9×10^{-17} N m^2.

In order to compare the bending stiffness of conventional cardiac tissue scaffolds[5-8], K_3, we used poly(lactic-co-glycolic acid) (PLGA) electro-spun fibers[4]

$$K_3 = E_{\mathrm{PLGA}} \frac{\pi d^4}{64} \tag{S3}$$

where E_{PLGA} is the Young's modulus of PLGA and d is the fiber diameter. When $E_{\mathrm{PLGA}} =$ 2 GPa[9, 10] and $d =$ 0.5, 1.0 and 1.5 μm[8, 11], we can calculate $K_3 =$ 6.1×10^{-18}, 9.8×10^{-17}, 5.0×10^{-16} N m^2, respectively.

The width and thickness of the SU-8/metal/SU-8 and SU-8 elements of the mesh have been chosen to have bending stiffness values of ca. 2.8×10^{-16} and 2.9×10^{-17} N m^2, respectively, that are comparable to that for 1 μm diameter PLGA electro-spun fibers, ca. 1.0×10^{-16} N m^2, used for cardiac tissue engineering[5-8]. These values together support the similarity in both dimensions and stiffness between nanoelectronic scaffolds and PLGA electro-spun fiber scaffolds. However, both are still highly limited in all the previously reported 3D electronics for interrogating tissues (Supplementary Table 1).

2. 3D tissue scaffold assembly

2.1 Assembly of 3D nanoelectronic scaffold

Key steps in the assembly of free-standing nanoelectronic scaffolds are as follows:

(1) The free-standing nanoelectronic mesh scaffold was rinsed three times with DI water and stored in DI water. The DI water was gradually replaced with isopropanol, which led to the nanoelectronic mesh scaffold being suspended in the isopropanol. The free-standing nanoelectronic mesh scaffold can be folded from this suspended configuration with 25 μm

DOI: 10.1038/NNANO.2016.96

thick or 50 μm thick or without an intervening passive scaffold films to control the inter-mesh layer separation. Cardiomyocyte seeding/culture (see Supplementary Methods, 3.2) and recording from beating nanoelectronics-cardiac tissue was achieved using different thickness PLGA eletrospun fiber films, although the data reported in this paper were focused on samples with 50 μm thick PLGA electro-spun fiber scaffold film (see Supplementary Methods, 2.2) spacers.

(2) The free-standing nanoelectronic mesh scaffold was folded from this suspended configuration by first placing an 25–50 μm thick PLGA electro-spun fiber films spacer over the 4 × 4 nanowire FET array closest to the I/O connector, and then flowing isopropanol towards I/O region (right to left in Supplementary Fig. 4a) to "flip" the free end of the mesh over the PLGA spacer layer.

(3) The isopropanol was then gradually replaced by DI water, which positioned the upper folded mesh structure at the air/water interface. Lowering the DI water level, while simultaneously using tweezer or micro-manipulator to position nanoelectronic mesh scaffold, allows the top folded layer of the mesh scaffold will be brought into contact with the PLGA/lower layer to complete one round of folding (Supplementary Fig. 4b). The device regions in each nanoelectronic mesh layer were aligned in *x* and *y* coordinates with the manual positioning accuracy controlled to better than 50 μm (verified by optical microscopy, Supplementary Fig. 4c). Employing a precise *x*-*y*-*z* micromanipulator for positioning would enable further improvement in the layer-to-layer alignment accuracy.

(4) The remaining water was allowed to visibly evaporate (5–15 min), and then the aligned and folded nanoelectronic mesh scaffold with intervening PLGA electro-spun fiber scaffold films was fixed to the substrate by applying silicone adhesive (Kwik-Sil, World Precision

Instruments, Inc., Sarasota, FL) at the two edges of the overlaid layers (Supplementary Fig. 4d).

(5) Isopropanol was added to re-suspend the remainder of mesh scaffold, and then steps (2) to (4) were repeated to fold the mesh scaffold into multiple layers with controlled *x-y-z* coordinates for all of the nanowire FET devices.

Representative images of a typical 4-layer/3-fold structure and a single mesh/PLGA layer are shown in Supplementary Figs. 4e–f, respectively. The overall geometry and 3D arrangement of devices can also be varied during the folding process. For example, the spacing between device layers can be controlled by the thickness of passive scaffold layers, and geometry can be further elaborated by folding over curved surfaces or rolling into cylindrical structures.

2.2 Electro-spinning PLGA fiber scaffold films

The PLGA electro-spun fiber films used in conjunction with the folded nanoelectronic scaffolds were prepared as follows. First, PLGA powder (PLGA, PURASORB PLG 1017, Purac Biomaterials, Lincolnshire, IL) was dissolved in hexafluoro-2-propanol (105228, Sigma-Aldrich Corporation, Atlanta, GA) with stirring for 3 days. The PLGA solution was loaded into a syringe connected to a 16-gauge needle (Sigma-Aldrich Corporation, Atlanta, GA) that was oriented perpendicular to a flat aluminum foil ground plane 20 cm away from the tip. 20 kV DC (Gamma High Voltage Research, Ormond Beach, FL) was applied between needle and aluminum foil, and the PLGA solution was delivered at a rate of 0.5 mL h^{-1} (Syringe pump, Harvard Apparatus, Holliston, MA). The Electro-spun PLGA films were collected on the aluminum foil and PLGA electro-spun fiber films were placed in a vacuum desiccator for at least two weeks prior to tissue culture to remove residual hexafluoro-2-propanol. For most studies, 50 μm thick PLGA electro-spun fiber films were used to yield a total 200 μm thick tissue scaffold for 4-layer/3-fold

DOI: 10.1038/NNANO.2016.96

nanoelectronic scaffold structures, which represents approximately the maximum thickness of engineered tissues without embedded vasculature[12].

3. Nanoelectronics-cardiac tissue

3.1 Preparation for tissue growth

A home-made printed-circuit-board (PCB) connector was mounted adjacent to the I/O region of nanoelectronic scaffolds, and then wire-bonding (West Bond Inc., Anaheim, CA) was used to connect the PCB connectors to the nanowire FET device I/O pads (Supplementary Fig. 5a).

A polystyrene petri-dish (Sterile, 35 mm diameter, 15 mm height, VWR Inc., Atlanta, GA) with a 10 × 10 mm^2 opening in the bottom was mounted on the substrate, to which the folded nanoelectronic scaffold is attached, using silicone adhesive (Kwik-Sil, World Precision Instruments, Inc., Sarasota, FL) (Supplementary Fig. 5b).

The petri-dish with folded nanoelectronic scaffold was sterilized by UV-light illumination for 0.5 h and subsequent soaking in 70% ethanol solution for 0.5 h, followed by oxygen plasma (50 W, 1 min) treatment. The nanoelectronic mesh scaffold was immersed in fibronectin/gelatin solution (0.5% fibronectin, F1141, Sigma-Aldrich Corporation, Atlanta, GA and 0.02% gelatin, Fisher Scientific, Pittsburgh, PA) for 2 h prior to cell culture.

3.2 Primary culture of cardiac tissues

Primary neonatal rat cardiomyocytes were prepared according to published procedures[2, 13]. Briefly, intact ventricles were isolated from 1–3 day old Sprague/Dawley rats and were then digested at 37 °C in Hanks' balanced salt solution (HBSS) containing 0.045% (*w*/*v*) collagenase (class II, Worthington Biochemical Corporation, Lakewood, NJ). Isolated cells were suspended in the culture medium comprising 5% fetal bovine serum (FBS) and 95% Medium 199 (Life

Technologies, Grand Island, NY), supplemented with 500 U mL^{-1} penicillin and 100 mg mL^{-1} streptomycin. The cell suspension was pre-plated in a flask for 2 h to reduce the percentage of non-cardiomyocyte cells. Then the collected supernatant was concentrated and counted on a hemocytometer. Cells were then plated at a density of 3–6 × 10^6 cm^{-2} onto the folded 4-layer nanoelectronic scaffolds, and incubated at 37 °C in a humidified atmosphere with 5% CO_2; the medium was changed every other day.

3.3 Tissue immunostaining

Nanoelectronics-cardiac tissue was fixed with 4% paraformaldehyde (Electron Microscope Sciences, Hatfield, PA) in PBS (1×, Corning Inc., NY) for 30 min, followed by 3× wash with ice-cold PBS. Tissue was permeabilized with 0.25% Triton X-100 in PBS for 1 h at room temperature, followed by 3× wash with ice-cold PBS, and pre-blocked with 10% FBS in PBS for 1 h at room temperature. Samples were incubated with primary antibodies in BlockAid solution (Molecular Probes, Invitrogen, Grand Island, NY) for 1 h at room temperature, followed by 3× wash with ice-cold PBS. Samples were then incubated with fluorophore-labeled secondary antibodies, followed by 3× wash with ice-cold PBS in the dark. Cell nuclei were counter stained with 0.2 μg mL^{-1} 4',6-diamidino-2-phenylindole (DAPI, Molecular Probes, Invitrogen, Grand Island, NY) for 1 min and then rinsed with PBS in the dark. Anti-sarcomeric α-actinin mouse monoclonal antibody (1:250; Clone EA-53, Sigma-Aldrich Corporation, Atlanta, GA) was used to label sarcomere in the nanoelectronics-cardiac tissue with AlexaFluor-488 goat anti-mouse (1:400; Molecular Probes, Invitrogen, Grand Island, NY) used as the secondary antibody. In order to visualize the nanoelectronic mesh scaffolds, the SU-8 component of the mesh was doped with 1 μg mL^{-1} rhodamine 6G (Sigma-Aldrich Corporation, Atlanta, GA) during PL.

3.4 Tissue imaging

DOI: 10.1038/NNANO.2016.96

Confocal imaging was carried out using an Olympus Fluoview FV1000 confocal laser scanning microscope. Confocal images were acquired using 405, 473 and 559 nm to excite components labeled with DAPI, AlexaFluor-488 and Rodamine 6G fluorescent dyes, respectively. ImageJ (ver. 1.48v, Wayne Rasband, National Institutes of Health) was used for 3D reconstruction and analysis of the confocal images. A representative confocal microscopy image of cardiac tissue obtained following culture in the 3D folded nanoelectronics scaffold for 7 days (Supplementary Fig. 6a) shows clearly the sarcomeric α-actinin of the cardiomyocytes (green) and the nanoelectronic SU-8 scaffold (red). Higher magnification images (Supplementary Figs. 6b–c) further exhibit partial alignment of cardiomyocytes along SU-8 backbones, and a sarcomere length, 2.1 ± 0.1 μm, characteristic of adult cardiomyocytes[14], demonstrating aligned development of the cardiac tissue cultured on 3D nanoelectronic scaffolds.

4. Electrophysiology measurements

4.1 3D spatiotemporal mapping of electrophysiology

Electrophysiology measurements were carried out at 37 °C (TC-344D temperature controller, Warner Instruments Corporation, Hamden, CT) in Tyrode solution (Sigma-Aldrich Corporation, Atlanta, GA). The conductance of silicon nanowire FETs was measured with DC bias set to 100 mV. The drain current was amplified with 16-channel-multiplexed preamplifier (SIM918 Precision current preamplifier, Stanford Research System) and the output data were band pass filtered (0–6000 Hz, home-built system) and recorded at an acquisition rate of 20–100 kHz using a 16-channel A/D converter (Digidata 1440A; Molecular Devices, Sunnyvale, CA) interfaced with a computer running pClamp 10.2 electrophysiology software (Molecular Devices, Axon Laboratory, Sunnyvale, CA). Data analysis was carried out using OriginPro (ver. 8.1, Origin Lab Corp.) and Matlab (ver. R2011a, Mathworks).

In order to estimate the measurement time-resolution, the response of the silicon nanowire FETs was characterized using previously reported pulsed water-gate method[15, 16]. Specifically, water-gate squared steps with variable rise time from 0.01–1000 ms were using a Ag/AgCl reference electrode. The 10%–90% rise time of the nanowire FET device conductance were calculated and compared to the water-gate pulse temporal variation. The time-resolution of the devices was found to be 0.01–0.05 ms.

4.2 Time-dependent 3D mapping of electrophysiology

Nanowire FET recording measurements were carried out at 2, 4, 6 and 8 days *in vitro* (DIV) in the same way as described in Supplementary Methods 4.1. The sensitivity and sensitivity-to-noise ratio of the devices were monitored over this period. The sensitivity shows a monotonic decrease as a function of culture time (Supplementary Figs. 7a,c); the sensitivity-to-noise ratio plotted as a function of culture time shows an increase up to day 4 and decrease after day 4, but shows consistently better performance than that measured before tissue culture (Supplementary Figs. 7b–c). Similar trends have also been reported in our previous work[17]. The eventual failure modes of silicon nanowire devices are likely due to the hydrolysis of silicon oxide in the physiological environment, containing chlorides and phosphates anions[18].

The mV amplitudes of recorded extracellular AP peaks were calibrated using the sensitivity of the individual devices, and can be compared directly. During the time-dependent measurement of electrophysiology, the nanowire sensors typically show less than 10% failure for up to 2 weeks (Supplementary Fig. 7d). In the context of long-term chronic recording, metal oxide passivated silicon nanowire sensors has achieved stable performance over one hundred days period under physiological environment[17].

4.3 Pharmacologically modulated electrophysiology

DOI: 10.1038/NNANO.2016.96

We have carried out dynamic mapping of AP propagation in 3D nanoelectronics-cardiac tissues under pharmacological modulation by norepinephrine and 1-heptanol addition. Drug responses were tested at 7 DIV with perfusion method for homogeneous delivery of drugs (Supplementary Figs. 10a and 11a), and 3D arrays of nanowire FET devices were simultaneously monitored.

4.3.1 Norepinephrine modulated electrophysiology

Norepinephrine (noradrenaline) has a positive chronotropic effect on cardiomyocytes through β-1 adrenergic receptors cardiac activation[2], which increases the depolarization and the heart beating rates. Tyrode medium containing 10 μM norepinephrine was delivered to entire tissue samples in a similar way (Supplementary Fig. 10a). Representative time-dependent traces recorded from four different layers (*L1–L4*) of the tissue before, immediately after and at steady-state 5 min following norepinephrine perfusion (Supplementary Fig. 10b) exhibit a beating rate increase of ~150%, consistent with the expected norepinephrine effect. Importantly, during the beating rate increase, the synchronization between APs recorded from different channels was fully maintained (Supplementary Fig. 10b), thus demonstrating functional tissue integrity in response to the homogeneous drug delivery.

Interestingly, isochronal maps of the time latency between different devices before, 30 s after and at steady-state 5 min following norepinephrine perfusion (Supplementary Fig. 10c) exhibit a transient increases of conduction velocity with AP propagation patterns unaltered. This phenomenon lasts only ca. 0–60 s following norepinephrine perfusion with peak conduction velocity increase at 30 s post drug delivery (of ~17%). This increase would be difficult to observe with methods that require averaging of AP peaks in order to resolve accurate time latency. The observed instability of conduction velocity could potentially lead to ventricle arrhythmogenesis[19], which has been neglected before.

4.3.2 1-heptanol modulated electrophysiology

1-heptanol, a gap-junction blocker[20], was used to inhibit intercellular gap-junctions used for electrotonic (cell-to-cell) current conduction. Tyrode medium containing 20 μM 1-heptanol was delivered to the entire nanoelectronics-cardiac tissue sample (Supplementary Fig. 11a). Representative time-dependent traces recorded from nanowire FET devices in different layers (*L1–L4*) of the tissue before and at steady-state 20 min following 1-heptanol perfusion (Supplementary Fig. 11b) highlight several key points. (1) The well-defined AP peaks are essentially unchanged following addition of 1-heptanol, which is consistent with this molecule functioning as a blocker of gap-junctions between cells[20]. (2) Analyses of the time latency between *L1–L2*, Δt_1, *L2–L3*, Δt_2 and *L3–L4*, Δt_3, before and after the 1-heptanol addition (Supplementary Fig. 11b) show a ~17% increase, which is also consistent with action of the added 1-heptanol. (3) The layer-to-layer AP propagation direction remained unchanged along with the uniform decrease of AP conduction velocity. In addition, examination of the full 3D latency maps recorded before and after 1-heptanol addition (Supplementary Fig. 11c) confirms the uniformity of the conduction velocity decrease, which correlates with uniform perfusion of gap-junction blocker, through the tissue.

The ability to determine AP conduction velocity with high-resolution at the single peak level without averaging, provides unique insight into drug diffusion in the tissue. Specifically, time latency changes Δt_1, Δt_2, Δt_3 plotted for the first 30 s following 1-heptanol addition (Supplementary Fig. 11d) show that the steady-state ~17% increase in latency is achieved in only 30 s, but that the onset of the latency increase varies from 8 to 10 s for *L1–L2*, to *L3–L4*. Importantly, these latter results show clearly our ability to monitor the diffusion and action of 1-heptanol from the top surface through the interior of the tissue in real-time. In comparison,

DOI: 10.1038/NNANO.2016.96

previous 3D optical imaging methods to visualize 3D dynamic changes require averaging multiple scans to achieve good resolution[21], and thus have difficulty in resolving such behavior in 3D cardiac tissue samples.

5. Active control of tissue electrophysiology

5.1 Electrodes for electrophysiology manipulation

Simultaneous control and monitoring of cardiac activity in the 3D nanoelectronics-cardiac tissue open up new opportunities for biological studies and nanoelectronics-biology communication. To this end, we have incorporate arrays of microelectrodes capable of stimulating cells into the nanoelectronic scaffolds. As an illustrative example, PL and metal deposition were used to pattern a 2 × 2 array palladium/platinum electrodes (50/50 nm) at four corners in *L4* of the nanowire FET arrays (Fig. 4a). Impedance/frequency (*Z–f*) data for the palladium/platinum electrodes were recorded in 1× PBS using an Agilent B1500A semiconductor device parameter analyzer (Agilent Technologies Inc., Santa Clara, CA) with B1520A-FG multi-frequency capacitance measurement unit (Agilent Technologies Inc., Santa Clara, CA). The typical impedance of the electrodes was below 100 kΩ at frequency of 1 kHz.

5.2 Simultaneous measurement and manipulation

Stimulation spikes used to control cardiac activity were biphasic squared pulses with 1 ms peak width, variable peak amplitudes and frequency, controlled by a 4-channel output D/A converter (Digidata 1440A; Molecular Devices, Sunnyvale, CA) interfaced with a computer running pClamp 10.2 electrophysiology software (Molecular Devices, Axon Laboratory, Sunnyvale, CA). Simultaneous recording from nanowire FET sensors before and during stimulation at 1.25 Hz and 1, 10, 100 mV (Supplementary Figs. 12a–d, respectively) and 1 V (Fig. 4b), as well as after

cessation of stimulation (Supplementary Fig. 12e) were carried out first. Results have shown that (1) the original beating rate of nanoelectronics-cardiac tissue, ca. 1 Hz, was not modulated by the 1.25 Hz stimulation with amplitude ≤100 mV (Supplementary Fig. 12f). This is evident from the absence of correlation between AP (blue asterisks) and stimulation peaks (red dashed-lines). (2) An increasing coefficient of variation of the beating rate was observed under increasing stimulation from 1 mV to 100 mV (Supplementary Fig. 12f), suggesting an increasing instability due to input electrical pulses. (3) When the stimulation voltage was increased to 1 V (Fig. 4b and Supplementary Fig. 12f), the APs recorded from all sensors are synchronized with the stimulation pulses as evidenced by the fixed delay between the stimulation peaks and corresponding AP peaks. (4) The pacing effect from electrical stimulation was reversible, as shown by the return of the beating to ca. 1 Hz once stimulation pulses were stopped.

The frequency range at which the 1 V stimulation peaks could be used to actively control the overall tissue beating frequency was tested by apply varying the frequency from 1.25 to 3.33 Hz (Fig. 4b; Supplementary Figs. 13). Representative real-time recording traces from nanowire FET sensors show clear temporal correlation between APs and stimulation spikes for 1.25 Hz (Fig. 4b and Supplementary Fig. 13c), 1.67 Hz (Supplementary Figs. 13a,c) and 2.5 Hz (Supplementary Figs. 13b–c), respectively. These results imply that it is possible to modulate cardiac activity by various frequency stimulations on demand, and thus could serve as a potential therapy for cardiac activity regulation.

DOI: 10.1038/NNANO.2016.96

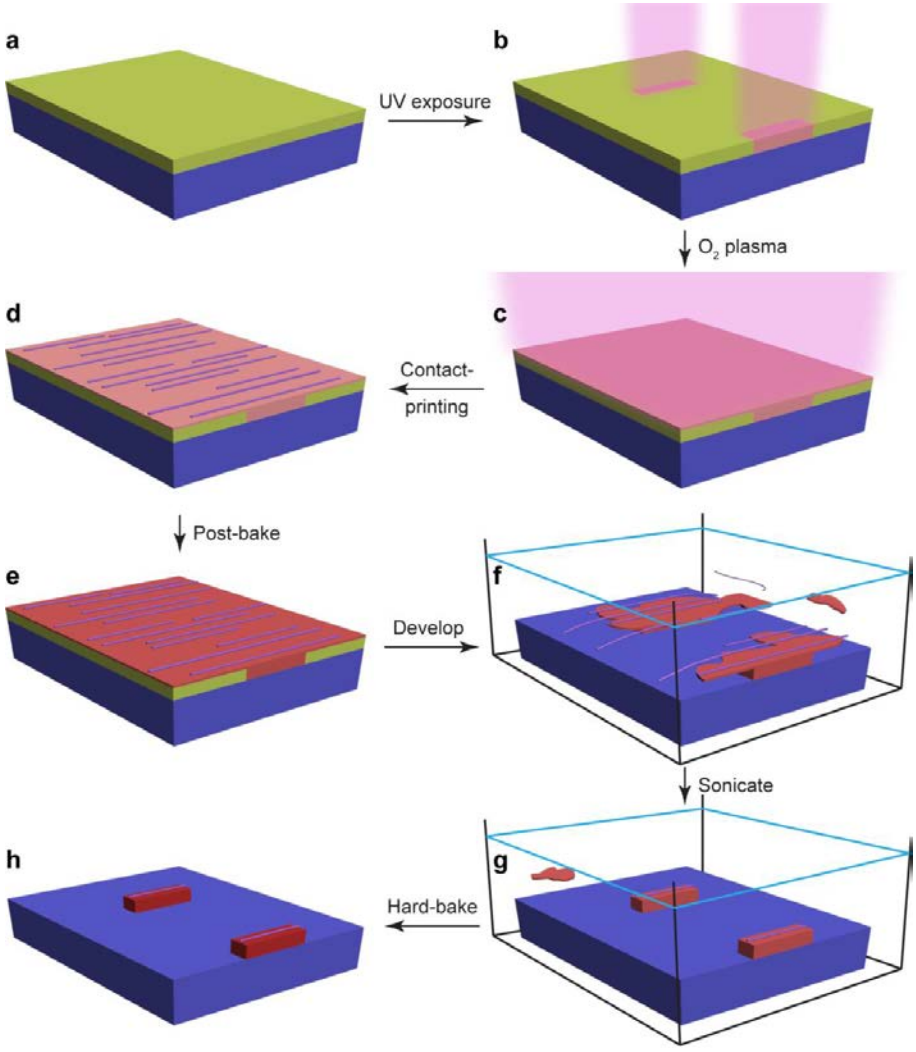

Supplementary Figure 1 | Nanowire contact printing on polymer. Schematics illustrating key steps in contact printing of silicon nanowires on SU-8 surfaces. (**a**) A layer of SU-8 photoresist was spin-coated and pre-baked. (**b**) Photolithography (PL) UV exposure was used to define an array of rectangular pads for nanowire assembly. (**c**) Gentle oxygen plasma was conducted to treat the surface of SU-8 photoresist. (**d**) Silicon nanowires on the growth substrate are transferred onto the surface of SU-8 through contact printing. (**e**) The substrate was post-baked to anchor the nanowires. (**f**) The substrate was placed in SU-8 developer for 1 min to remove the

non-crosslinked regions. (**g**) Gentle sonication was carried out to break and remove the free-standing segments of nanowires and SU-8 thin films. (**h**) Substrate was hard-baked at 180 °C for 20 min.

DOI: 10.1038/NNANO.2016.96

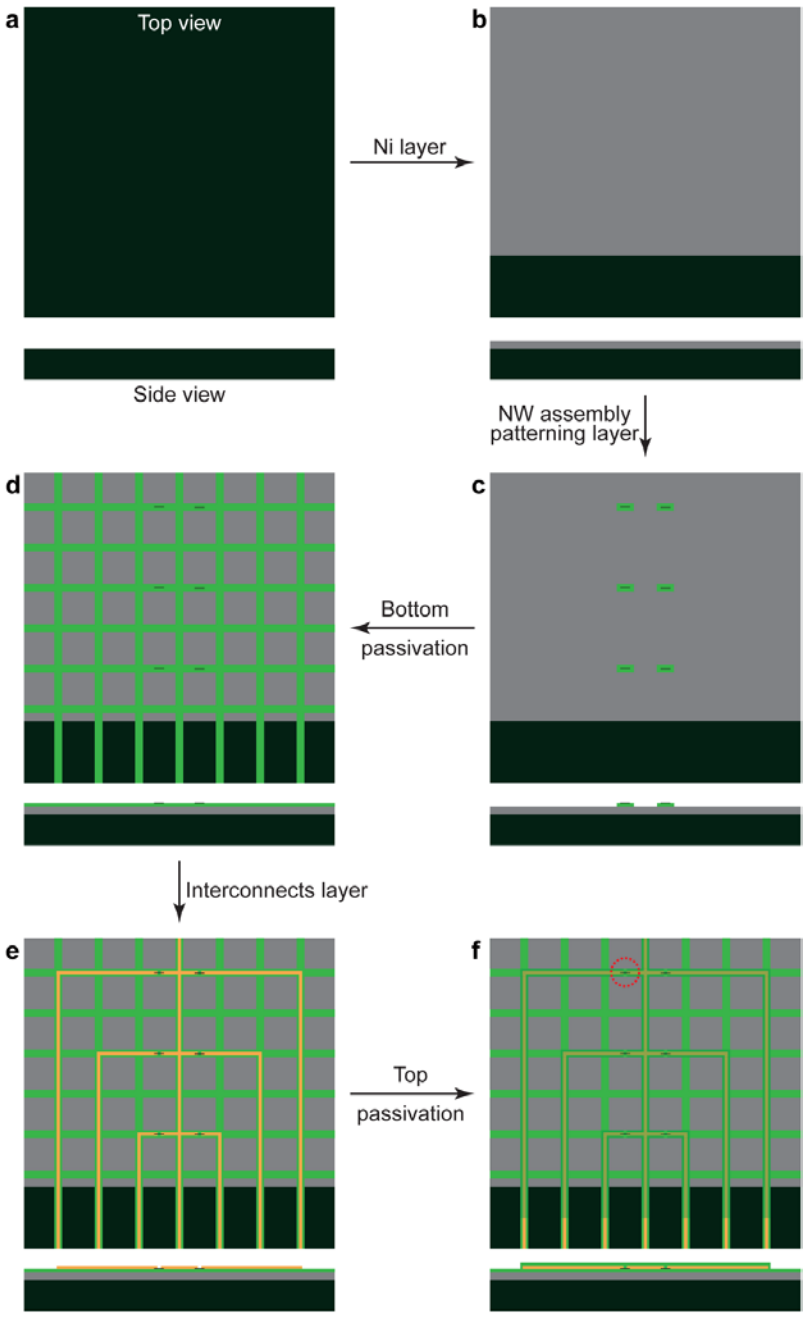

Supplementary Figure 2 | Nanoelectronic mesh fabrication scheme. Components include silicon wafer (dark green), nickel relief layer (silver), SU-8 polymer ribbons (light green), metal interconnects (yellow) and silicon nanowire (black). For each step a top-view and side-view are

shown. The nanowire assembly patterning layer is an array of rectangular SU-8 pads with 350 nm thickness, 4 μm width and 20 μm length. The bottom and top SU-8 passivation layers defined by photolithography are 4 μm in width and 350 nm in thickness. The metal source/drain interconnects deposited by thermal evaporator are Cr/Pd/Cr, 2 μm in width and 1.5/50/1.5 nm in thickness. The red circle in (**f**) denotes the position of one silicon nanowire sensor. More details are described in the Supplementary Methods, 1.3.

DOI: 10.1038/NNANO.2016.96

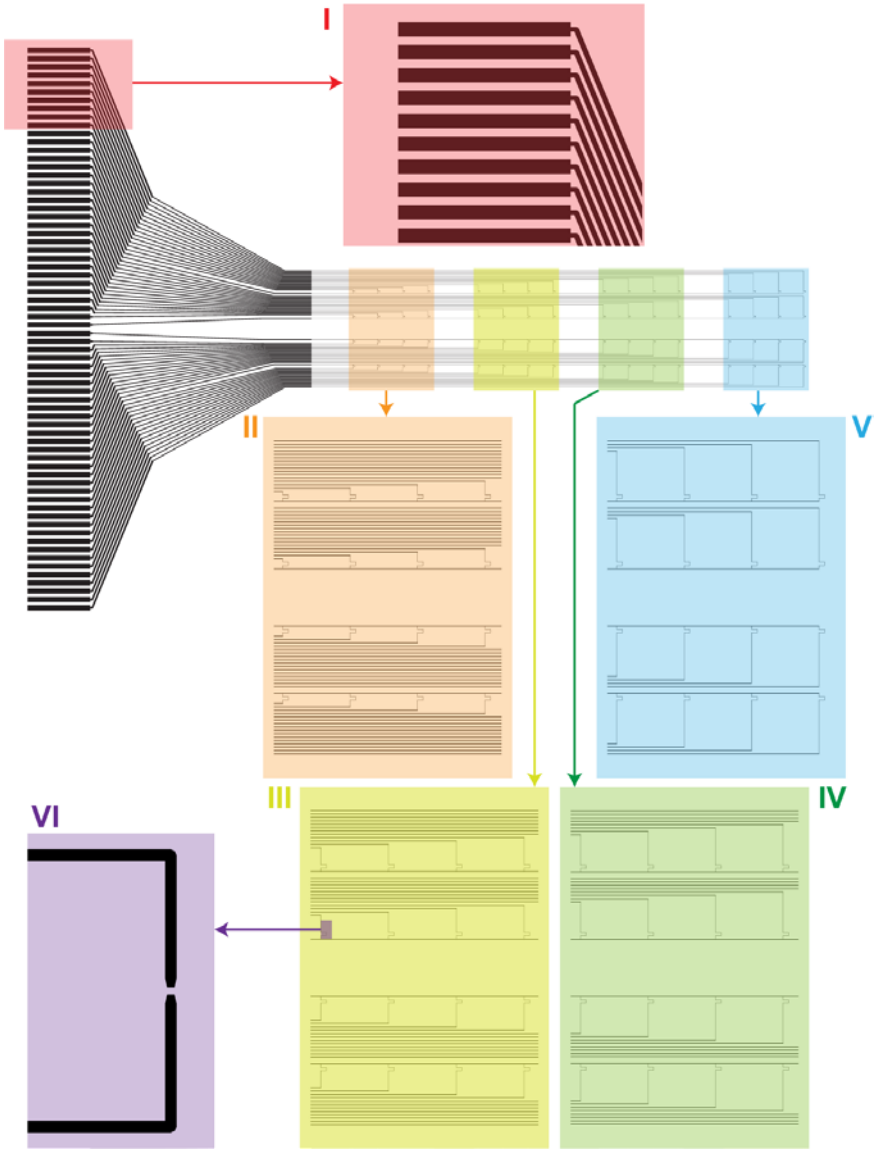

Supplementary Figure 3 | Nanoelectronic mesh layouts. The layout of interconnects for 64 nanowire FET sensors. Inset I: Zoom-in layout of the input/output (I/O) region. Insets II–V: Zoom-in layouts of four nanowire FET sensor regions, each containing 4 × 4 devices. Inset VI: Zoom-in layout of single nanowire FET sensor. Gap between metal source/drain contacts is 2 μm × 2 μm. The layouts of the scaffolds can be easily changed by re-designing various lithography masks without affecting the basic principles of the whole fabrication strategies.

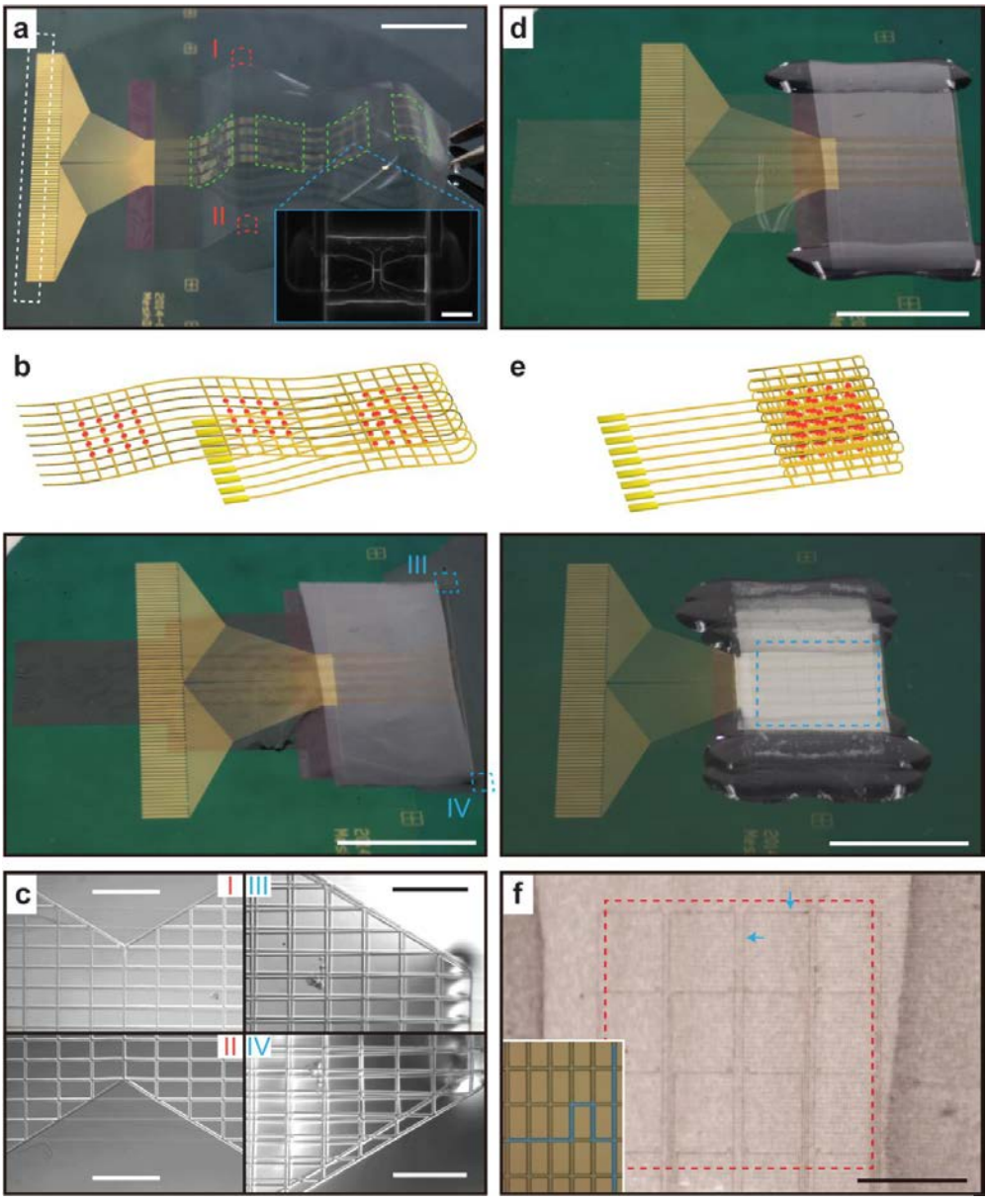

Supplementary Figure 4 | Folding processes to form 3D nanoelectronic scaffolds. (**a**) Photograph of an as-fabricated free-standing nanoelectronic mesh scaffold with 4 sets of 4×4 arrays containing at total of 64 addressable nanowire FET sensors suspended in deionized (DI) water. Scale bar, 1 cm. White dashed-box highlights the I/O metal electrode pads for connection with external instruments. Green dashed-boxes highlight the four 4 × 4 device array regions each

DOI: 10.1038/NNANO.2016.96

consisting of 16 nanowire FET sensors. Red dashed-boxes I and II highlight the upper and lower boundaries of first folding line. Zoom-in of these two regions will be shown in (**c**). Inset: dark-field microscopy image of one individual FET sensor. Scale bar, 2 μm. (**b**) Schematic (top) and photograph (bottom) showing the first folding step with two layers of the nanoelectronic mesh layers separated by a 50 μm thick poly(lactic-co-glycolic acid) (PLGA) electrospun fiber film (light grey, vertically-oriented rectangle at right of image). Scale bar, 1 cm. Blue dashed-boxes III and IV highlight the upper and lower boundaries of first folding line. Zoom-in of these two regions will be shown in (**c**). (**c**) 20× magnification optical images of nanoelectronic mesh before (I and II) and after (III and IV) first folding. Alignment accuracy as shown in III and IV is <50 μm. Scale bar, 200 μm. (**d**) Photograph showing upper and lower edges of the folded nanoelectronic mesh layers were fixed with Kwik-Sil silicone adhesive at the upper and lower edges. Scale bar, 1 cm. (**e**) Schematic (top) and photograph (bottom) showing nanoelectronic mesh folded three times (four mesh layers) with upper and lower edges fixed as noted in (**d**). Scale bar, 1 cm. (**f**) Zoomed-in image of blue dashed-box in (**e**) showing the nanoelectronic scaffold lying on the electro-spun PLGA fiber film. Gray vertical/horizontal lines (highlighted by blue arrows) correspond to the SU-8/metal/SU-8 mesh elements; SU-8 elements without metal are not visible. Scale bar, 2.5 mm. Inset: Bright-field optical microscopy image of ~100 μm × 120 μm region shows the SU-8 ribbon with metal (false-colored in blue) and without metal lines.

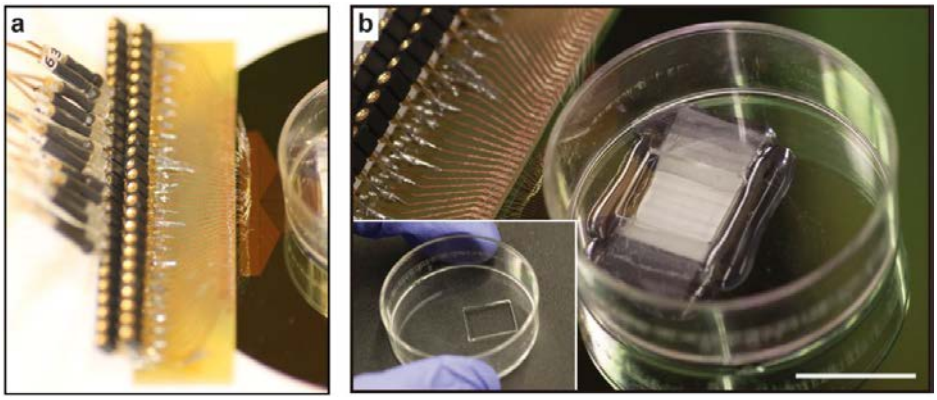

Supplementary Figure 5 | Chip preparation for tissue culture. (**a**) Photograph of a home-made PCB connector mounted adjacent to the I/O region of nanoelectronic scaffolds and then wire-bonded to the nanowire FET device I/O pads. (**b**) Photograph of modified petri dish with ~10 × 10 mm^2 opening mounted on the scaffold substrate using Kwik-Sil silicone adhesive (see Supplementary Methods, 3.1). Inset: Modified petri dish with opening in the bottom. Scale bar, 1 cm.

DOI: 10.1038/NNANO.2016.96

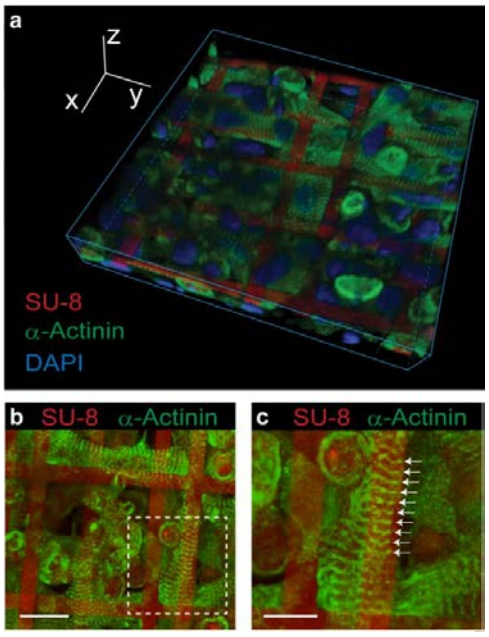

Supplementary Figure 6 | Confocal images of nanoelectronics-cardiac tissues. (**a**) Reconstructed 3D confocal microscopy image of a nanoelectronics-cardiac tissue sample. Scale bar, 25 μm. The nanoelectronic scaffold is labeled in red by rhodamine 6G. Cardiomyocyte sarcomeric α-actinin and cell nuclei are stained in green and blue, respectively. (**b**) Confocal microscopy image of cardiomyocytes grown within the nanoelectronic scaffold. Scale bar, 20 μm. (**c**) A zoomed-in confocal microscopy image of white dashed-box in (**b**) showing a characteristic sarcomere length of 2.1 ± 0.1 μm. Scale bar, 10 μm.

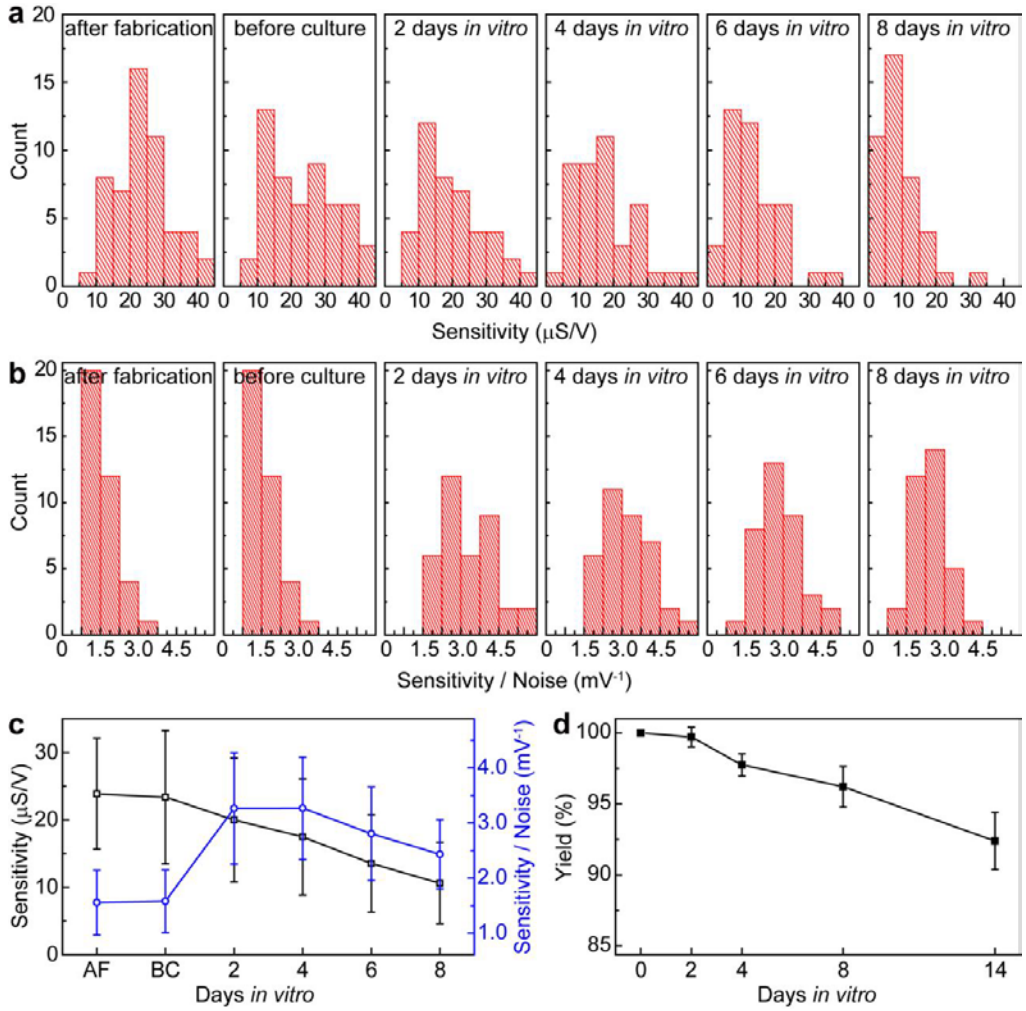

Supplementary Figure 7 | Nanowire FET sensor performance and stability. (**a**) Histograms of the sensitivity of the nanowire FET sensors measured after fabrication, after folding and preparation processes and before tissue culture, 2 days post tissue culture, 4 days post tissue culture, 6 days post tissue culture, 8 days post tissue culture. (**b**) Histograms of sensitivity-to-noise ratio of the nanowire FET sensors measured after fabrication, after folding and preparation processes and before tissue culture, 2 days post tissue culture, 4 days post tissue culture, 6 days post tissue culture, 8 days post tissue culture. (**c**) Plot showing the variations of sensitivity (black) and sensitivity-to-noise ratio (blue) as a function of tissue culture time (AF means after fabrication; BC means before culture). Error bars correspond to ± standard deviation. The sensitivity-to-noise ratio of the nanowire sensors shows enhanced performance during tissue

DOI: 10.1038/NNANO.2016.96

culture up to 8 days. (**d**) Plot showing the change of viable ratio of nanowire FET sensors as a function of tissue culture time. Error bars correspond to ± standard deviation. The nanowire sensors show less than 10% failure during tissue culture. Extended use times in excess of three months can be achieved by employing oxide shell coatings as described previously[17].

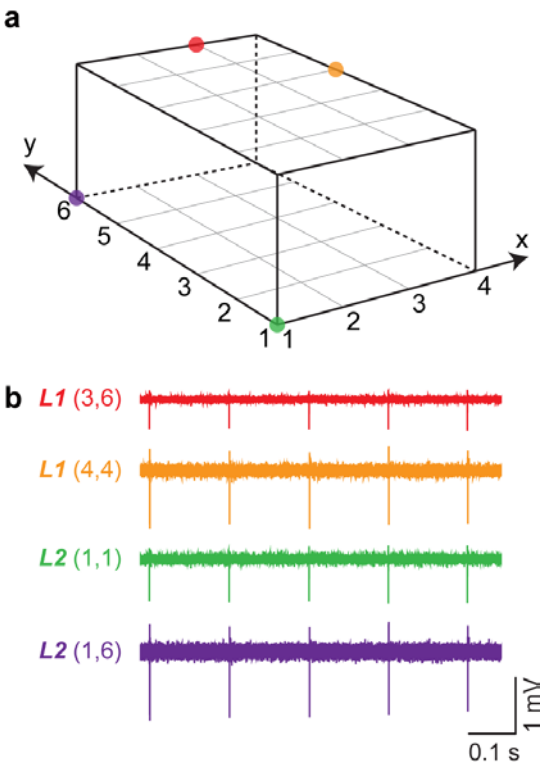

Supplementary Figure 8 | Synchronized beating at 2 days *in vitro* (DIV). Representative recording of action potentials (APs) sequences from four sensors at 2 DIV in the same nanoelectronics-cardiac tissue sample as shown in Fig. 2. (**a**) Four dots corresponding to the relative positions of the four selected sensors distributed in two layers. (**b**) Multiplexed recording traces from the four selected sensors showing synchronization of APs.

DOI: 10.1038/NNANO.2016.96

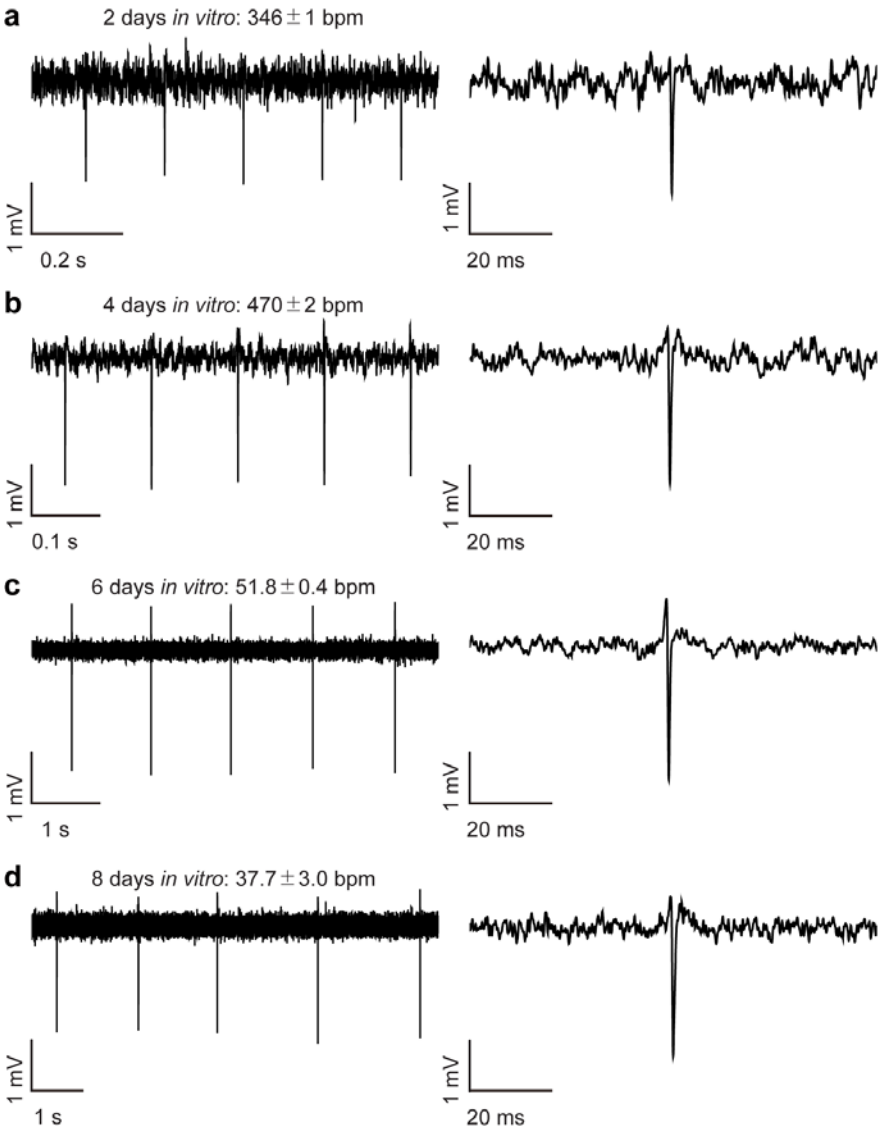

Supplementary Figure 9 | AP recorded at different DIV. Representative traces of APs recorded from 3D developing cardiac tissue (left) and typical individual spike (right) at 2 (**a**), 4 (**b**), 6 (**c**) and 8 (**d**) DIV. The beating rates were 346 ± 1, 470 ± 2, 51.8 ± 0.4 and 37.7 ± 3.0 per minute, respectively. The traces shown were recorded from same sensor in *L2*.

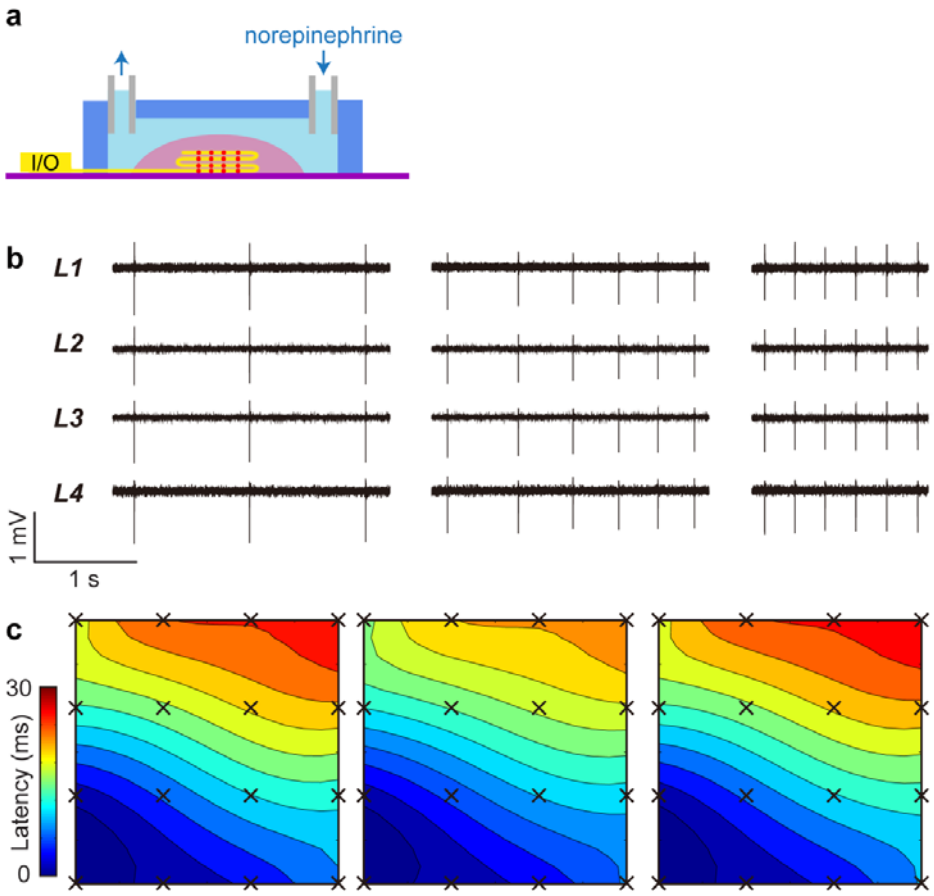

Supplementary Figure 10 | Nanoelectronics-cardiac tissue norepinephrine response. (**a**) Schematic of norepinephrine perfusion and measurement setup. (**b**) Representative multiplexed recordings of synchronized APs from four devices chosen from each of the four layers (*L1–L4*) in the nanoelectronics-cardiac tissue before, right after and 5 min after initiating the perfusion of Tyrode medium containing 10 μM norepinephrine. The beating rate continuously increases following norepinephrine perfusion and stabilizes at 150%. Importantly, during the beating rate increase, the synchronization between APs recorded from different channels was fully maintained, thus demonstrating functional tissue integrity in response to the homogeneous drug delivery. (**c**) Isochronal maps of time latency in single layer before, ca. 30 s after and 5 min after initiating the norepinephrine perfusion. Interestingly, these isochronal time latency maps exhibit a transient increase of conduction velocity with AP propagation patterns unaltered. This phenomenon lasts only ca. 0–60 s following norepinephrine perfusion with peaked conduction

DOI: 10.1038/NNANO.2016.96

velocity increase at 30 s post drug delivery (by ~17%). This increase would be difficult to observe with methods that require averaging of AP peaks in order to resolve accurate time latency.

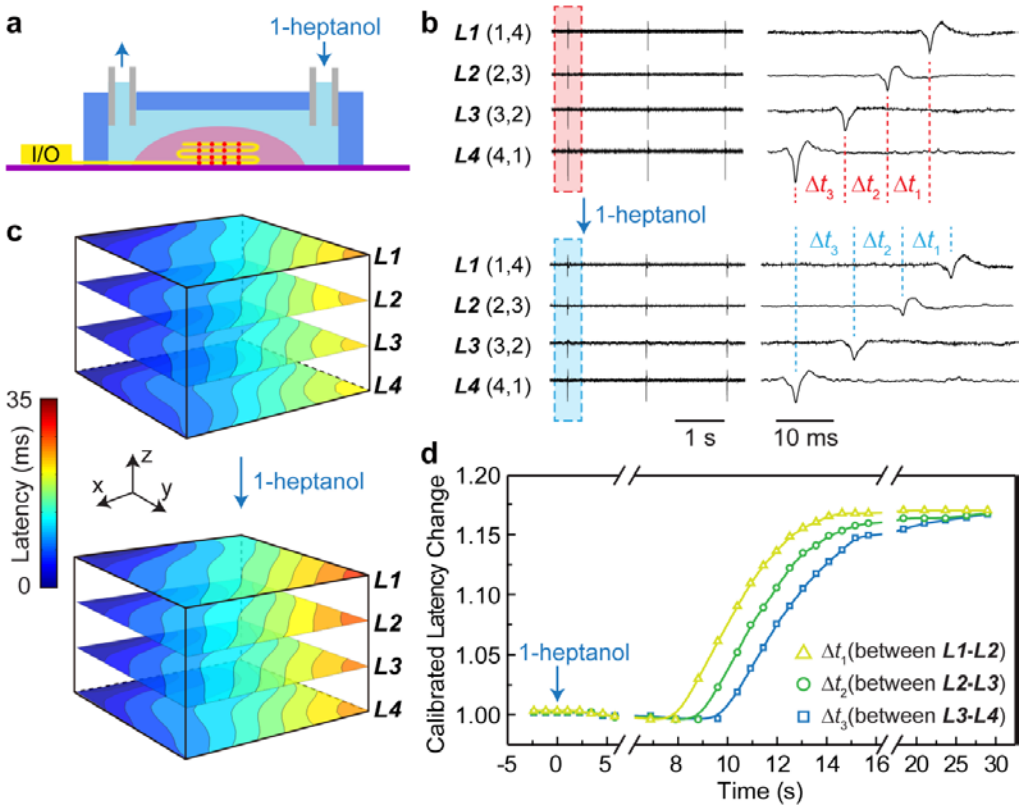

Supplementary Figure 11 | 3D mapping of 1-heptanol modulated electrophysiology. (**a**) Schematic of 1-heptanol perfusion and measurement setup. (**b**) Representative time-dependent traces recorded from nanowire FET devices in different layers (*L1–L4*) of the tissue before and at steady-state 20 min following 1-heptanol perfusion highlight several key points. (1) The well-defined AP peaks are essentially unchanged following addition of 1-heptanol, which is consistent with this molecule functioning as a blocker of gap-junctions between cells[20]. (2) Analyses of the time latency between *L1–L2*, Δt_1, *L2–L3*, Δt_2 and *L3–L4*, Δt_3, before and after the 1-heptanol addition show a ~17% increase, which is also consistent with action of the added 1-heptanol. (3) The layer-to-layer AP propagation direction remained unchanged along with the uniform decrease of AP conduction velocity. (**c**) 3D isochronal maps of time latency

DOI: 10.1038/NNANO.2016.96

before (top) and after (bottom) adding 1-heptanol confirm the uniformity of the conduction velocity decrease, which correlates with uniform perfusion of gap-junction blocker, through the tissue. The ability to determine AP conduction velocity with high-resolution at the single peak level without averaging, provides unique insight into drug diffusion in the tissue. (**d**) Dynamic changes of the latency Δt_1, Δt_2, Δt_3 between four representative devices versus time before and after adding 1-heptanol. Specifically, time latency changes Δt_1, Δt_2, Δt_3 plotted for the first 30 s following 1-heptanol addition show that the steady-state ~17% increase in latency is achieved in only 30 s, but that the onset of the latency increase varies from 8 to 10 s for *L1–L2*, to *L3–L4*. Importantly, these latter results show clearly our ability to monitor the diffusion and action of 1-heptanol from the top surface through the interior of the tissue in real-time.

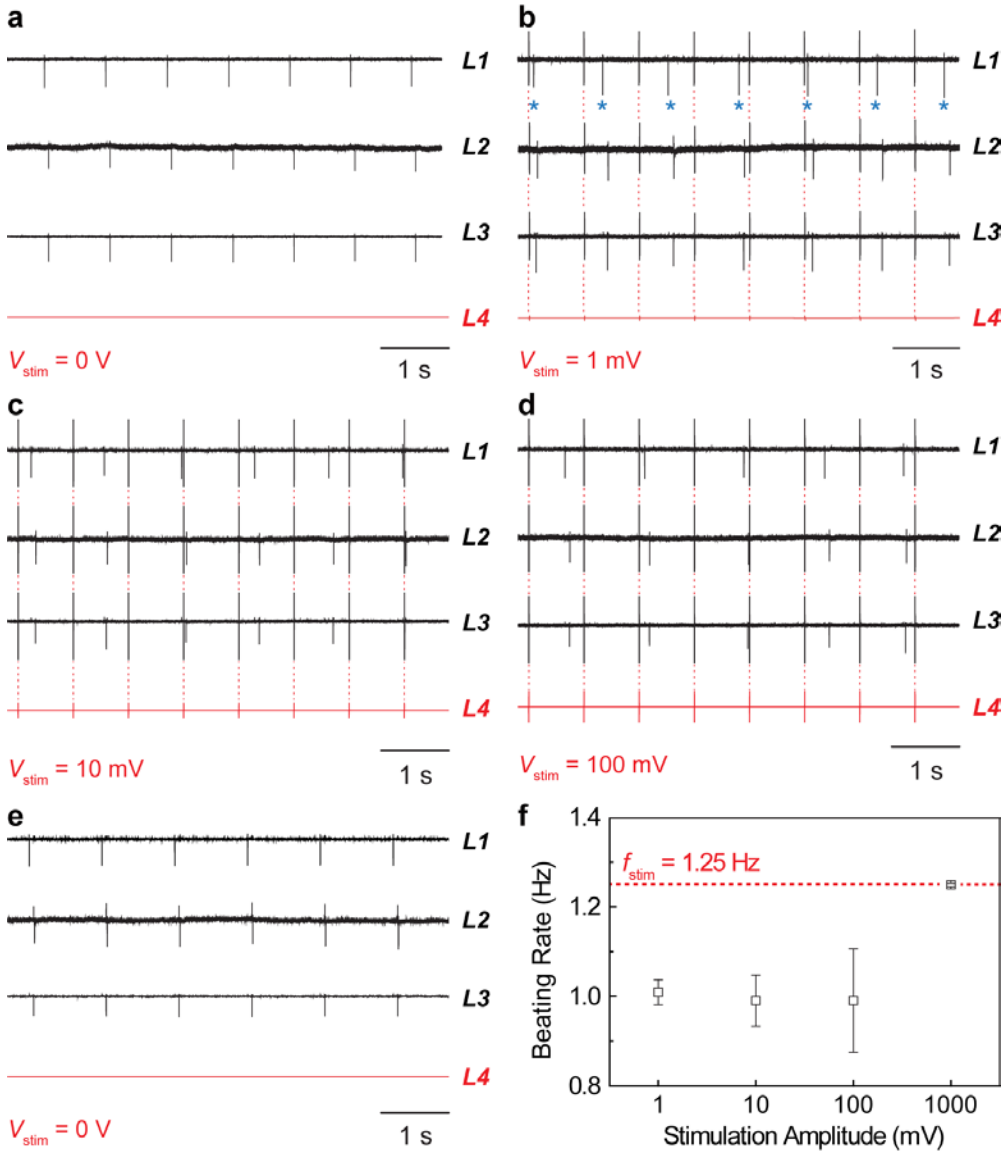

Supplementary Figure 12 | Regulation of APs with an integrated stimulator. (**a**) Representative multiplexed recordings of APs from nanowire FETs in *L1, L2*, *L3* (black traces) before applying stimulation; the beating rate is ~1.0 Hz. The device coordinates in the 4 × 4 arrays are *L1*(1,1), *L2*(4,4), *L3*(4,1). (**b–d**) Representative multiplexed recordings of APs from nanowire FETs in *L1, L2*, *L3* (black traces) and the periodic stimulation peaks (red trace). Stimulation peak width and frequency were 1 ms and 1.25 Hz, respectively. The stimulation amplitude in (**b**), (**c**) and (**d**) were 1, 10 and 100 mV, respectively. The stimulator is near *L4*(4,4).

DOI: 10.1038/NNANO.2016.96

Red dashed lines align the stimulation peaks with "artifact" spikes recorded from sensors due to capacitive coupling; recorded AP peaks (primarily downward peaks) occur at distinct times. (**e**) Representative multiplexed recordings of APs from same sensors after stopping the stimulation; the data show that nanoelectronics-cardiac tissue has recovered to its original beating rate of ~1.0 Hz. (**f**) Plot showing the beating rate as a function of stimulation amplitude; error bars correspond to ± standard deviation. The relative standard deviation (coefficient of variation) under increasing stimulation amplitudes from 1 mV to 1 V are 2.7%, 5.8%, 11.7% and 0.3%, respectively. The stimulation frequency was 1.25 Hz in all experiments. Results show that (1) the original beating rate of nanoelectronics-cardiac tissue, ca. 1 Hz, was not modulated by the 1.25 Hz stimulation for amplitudes ≤100 mV. The absence of modulation of the AP by stimulation is evident from the lack of correlation between AP (blue asterisks) and stimulation peaks (red dashed-lines). (2) An increasing coefficient of variation of the beating rate was observed under increasing stimulation from 1 to 100 mV (**f**), suggesting an increasing instability due to input electrical pulses. (3) When the stimulation voltage was increased to 1 V (Fig. 4b), the APs recorded from all sensors are synchronized with the stimulation pulses as evidenced by the fixed delay between the stimulation peaks and corresponding AP peaks. (4) The pacing effect from electrical stimulation was reversible, as shown by the return of the beating to ca. 1 Hz once stimulation pulses were stopped.

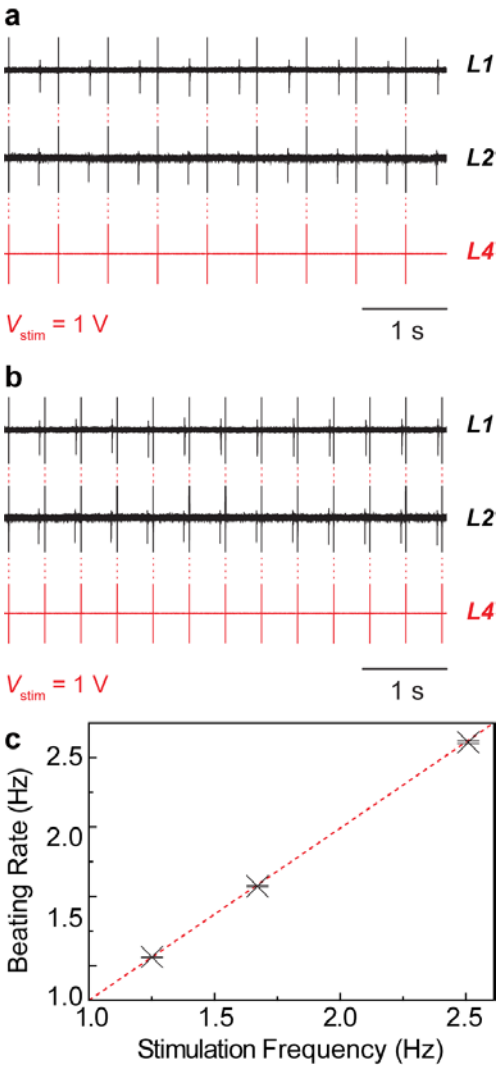

Supplementary Figure 13 | Regulation of APs with different stimulation frequencies. (**a–b**) Representative multiplexed time-dependent data recorded from *L1* and *L2* (black traces) and periodic stimulation peaks (red trace) at a stimulation frequencies of (**a**) 1.67 and (**b**) 2.50 Hz. Red dashed lines align the stimulation peaks with "artifact" spikes recorded from sensors due to capacitive coupling; recorded AP peaks (primarily downward spikes) occur at distinct times. The fixed time difference of the AP peaks relative to the stimulation peaks signify the lock to the stimulator input. The device coordinates are *L1*(1,2), *L2*(3,1) and the stimulator is near *L4*(4,4).

DOI: 10.1038/NNANO.2016.96

Supplementary Table. 1. Bending stiffness values of flexible electronics targeting 3D tissues.

Materials	System	Thickness (μm)	Width (μm)	Bending stiffness (N m)
PLGA electro-spun fibers[5-10] *	3D engineered cardiac tissue and bone tissue	1.0 (diameter)		9.8×10^{-17}
(1) SU-8 (2) SU-8/Pd/SU-8 †	3D engineered cardiac tissue	(1) 0.35 (2) 0.35/0.05/0.35	(1) 4.0 (2) 4.0/1.0–2.0/4.0	(1) 2.9×10^{-17} (2) $0.9–1.8 \times 10^{-16}$
(1) SU-8 (2) SU-8/Pd/SU-8 in PLGA electro-spun fibers[2] ‡	3D engineered cardiac tissue and smooth muscle tissue	(1) 2.0 (2) 2.0/0.075/2.0	(1) 40 (2) 40/20/40	(1) 5.3×10^{-14} (2) 4.5×10^{-13}

Note: * PLGA electro-spun fibers are mostly widely used for cardiac tissue and bone tissue engineering. Commonly used fiber diameter ranges from 0.8 to 1.5 μm, providing a bending stiffness value at ca. 9.8×10^{-17} N m for other ultra-flexible electronics to compare with.

† Tissue-scaffold-mimicking nanoelectronics reported in this study. Two constituent structural elements exhibit bending stiffness at $2.9 \times 10^{-17}$and $0.9–1.8 \times 10^{-16}$ N m, truly mimicking the natural cell-scaffold interaction with modified fibronectins that bind to cell membrane spanning integrins.

‡ Study based on SU-8 flexible electronics hybridized with PLGA eletro-spun fibers that achieved *in vitro* tissue engineering. However, the electronics components have one order of magnitude larger dimension and three orders of magnitude larger bending stiffness compared to the majority PLGA fiber components.

Supplementary References

1. Patolsky, F., Zheng, G. & Lieber, C.M. Fabrication of silicon nanowire devices for ultrasensitive, label-free, real-time detection of biological and chemical species. *Nature Protocols* **1**, 1711-1724 (2006).

2. Tian, B.Z. et al. Macroporous nanowire nanoelectronic scaffolds for synthetic tissues. *Nat Mater* **11**, 986-994 (2012).

3. Liu, J. et al. Multifunctional three-dimensional macroporous nanoelectronic networks for smart materials. *P Natl Acad Sci USA* **110**, 6694-6699 (2013).

4. Steif, P.S. Mechanics of materials. (Pearson, Upper Saddle River, NJ; 2012).

5. Eschenhagen, T. & Zimmermann, W.H. Engineering myocardial tissue. *Circ Res* **97**, 1220-1231 (2005).

6. Dvir, T., Timko, B.P., Kohane, D.S. & Langer, R. Nanotechnological strategies for engineering complex tissues. *Nat Nanotechnol* **6**, 13-22 (2011).

7. Place, E.S., George, J.H., Williams, C.K. & Stevens, M.M. Synthetic polymer scaffolds for tissue engineering. *Chem Soc Rev* **38**, 1139-1151 (2009).

8. Zong, X.H. et al. Electrospun fine-textured scaffolds for heart tissue constructs. *Biomaterials* **26**, 5330-5338 (2005).

9. Gentile, P., Chiono, V., Carmagnola, I. & Hatton, P.V. An Overview of Poly(lactic-co-glycolic) Acid (PLGA)-Based Biomaterials for Bone Tissue Engineering. *Int J Mol Sci* **15**, 3640-3659 (2014).

10. Rezwan, K., Chen, Q.Z., Blaker, J.J. & Boccaccini, A.R. Biodegradable and bioactive porous polymer/inorganic composite scaffolds for bone tissue engineering. *Biomaterials* **27**, 3413-3431 (2006).

11. Meng, Z.X. et al. Electrospinning of PLGA/gelatin randomly-oriented and aligned nanofibers as potential scaffold in tissue engineering. *Mat Sci Eng C-Mater* **30**, 1204-1210 (2010).

12. Lovett, M., Lee, K., Edwards, A. & Kaplan, D.L. Vascularization strategies for tissue engineering. *Tissue engineering. Part B, Reviews* **15**, 353-370 (2009).

13. Cohen-Karni, T., Timko, B.P., Weiss, L.E. & Lieber, C.M. Flexible electrical recording from cells using nanowire transistor arrays. *P Natl Acad Sci USA* **106**, 7309-7313 (2009).

14. Zhang, D. et al. Tissue-engineered cardiac patch for advanced functional maturation of human ESC-derived cardiomyocytes. *Biomaterials* **34**, 5813-5820 (2013).

DOI: 10.1038/NNANO.2016.96

15. Fu, T.M. et al. Sub-10-nm intracellular bioelectronic probes from nanowire-nanotube heterostructures. *P Natl Acad Sci USA* **111**, 1259-1264 (2014).

16. Duan, X. et al. Intracellular recordings of action potentials by an extracellular nanoscale field-effect transistor. *Nat Nanotechnol* **7**, 174-179 (2012).

17. Zhou, W. et al. Long Term Stability of Nanowire Nanoelectronics in Physiological Environments. *Nano Letters* **14**, 1614-1619 (2014).

18. Yin, L. et al. Mechanisms for hydrolysis of silicon nanomembranes as used in bioresorbable electronics. *Adv Mater* **27**, 1857-1864 (2015).

19. Myles, R.C., Wang, L.G., Kang, C.Y., Bers, D.M. & Ripplinger, C.M. Local beta-Adrenergic Stimulation Overcomes Source-Sink Mismatch to Generate Focal Arrhythmia. *Circ Res* **110**, 1454-1464 (2012).

20. Natarajan, A. et al. Patterned cardiomyocytes on microelectrode arrays as a functional, high information content drug screening platform. *Biomaterials* **32**, 4267-4274 (2011).

21. Hou, J.H., Kralj, J.M., Douglass, A.D., Engert, F. & Cohen, A.E. Simultaneous mapping of membrane voltage and calcium in zebrafish heart in vivo reveals chamber-specific developmental transitions in ionic currents. *Front Physiol* **5**, Doi 10.3389/Fphys.2014.00344 (2014).